Innovative 3D Printing of Mechanoluminescent Composites: Digital Light Processing Meets Machine Learning

Junheui Jo[a†], Kundo Park[a,b†], Hyunggwi Song[a,c†] and Seunghwa Ryu[a]

[a]*Department of Mechanical engineering, Advanced Institute of Science and Technology (KAIST), 291 Daehakro, 34141, Yuseonggu, Daejeon, Korea, Republic of Korea*

[b]*Department of Mechanical Engineering, University of California Berkeley, CA, 94720, Berkeley*

[c]*Ground technology research institute, Agency for Defense Development, Daejeon 34060, Republic of Korea*

Abstract

Mechanoluminescent (ML) materials, which refers to a class of material that emits light when subjected to external mechanical stimuli, have been drawing attention due to its unique multifunctionality, and potential applicability as a next-generation structural health monitoring technique. Nevertheless, the applicability of ML materials in real-world scenarios have been significantly confined due to its limitations, such as there is no universally accepted rules or framework for producing ML composites with high intensity, and the difficulty in producing the material in complex 3D shapes. As a breakthrough, here we present a novel approach where $SrAl_2O_4$:Eu^{2+}, Dy^{3+} particle-based mechanoluminescent composite is produced via digital light processing (DLP)-based 3D printing, whose process parameters are optimized through a machine learning-based optimization algorithm. In this study, we adopt multi-objective Bayesian optimization (MBO) to optimize the three salient process parameters of DLP-based additive manufacturing; ML particle content, layer thickness, and cure ratio, to achieve both strong ML properties and short printing time. Gaussian process regression is used for the modeling of complex input-output relationship, and the training data is collected by performing actual experiments. As a result, the pareto-optimal process parameter solutions determined by MBO not only allowed us to produce the high-performance ML specimens in short time, but they also allowed us to empirically understand how the process parameters affect the end product's ML property and the overall printing time. Furthermore, we validated the real-life applicability of our framework by applying the optimized DLP-based 3D printing framework to produce and test the ML-based stress sensors and ML-based mechanical components.

---

1. Introduction

As the demand for materials capable of addressing multiple challenges simultaneously continues to grow in modern industries, the focus of material researchers is increasingly directed towards multifunctional materials. Multifunctional materials literally denote a class of material that can perform multiple functions in a system due to their unique multi- physical properties, one of which is typically structural and the other functional, such as electrical, optical, thermal[1,2]. Mechanoluminescent (ML) composite refers to a special category of multifunctional materials that is capable of emitting light when subjected to external mechanical stimuli[3-5]. The ML composites are typically synthesized by uniformly and carefully distributing the ML particles (e.g. ZnS:Cu, $SrAl_2O_4:Eu^{2+}$) into a liquid-state matrix, and then hardening the mixture. The unique multifunctionality of ML composites initiated numerous research trying to understand the underlying principle of the phenomena and even apply it for the development of new engineering composites.

ML composites hold significant potential for diverse industrial applications. In structural engineering, they can serve as innovative technique for non-destructive testing, enabling the real-time detection of stress-induced damage or fatigue cracks in critical infrastructure like bridges, buildings, and aerospace components[6, 7]. Additionally, ML materials find applications in sensors, where their ability to respond to mechanical stimuli offers valuable insights into material behavior under varying conditions[8, 9]. As this field of research continues to advance, ML materials are poised to play an increasingly significant role in various modern industries, offering novel solutions for monitoring and sensing.

Nevertheless, there exists a technical hurdle that confines the practical application of ML composites in real-world scenarios: there is no universally accepted rules or framework for

producing ML composites with high intensity[4, 10]. It is no secret that 'high luminosity' is an essential prerequisite that an ML composite must have for them to be more actively adopted in real industries. Unfortunately, the underlying mechanism of how the ML materials can transduce the mechanical energy into photonic energy is not clearly identified yet. Due to the absence of an in-depth understanding on the relationship between the material design/production parameters and the resultant ML performance, there is no standardized way of optimally designing the ML composite's composition and the production process to achieve a high ML intensity.

Existing studies on improving the applicability of ML composites can be generally divided into two main categories. The first is to discover and modify the compositions of ML particles. The most noticeable discovery in this category was made by Zhang et al. who reported that the ML intensity of $SrAl_2O_4:Ce^{3+}$ is dramatically increased by co-doping the particle with 1.5% of Ho^{3+}[11]. The idea of co-doping has been extensively adopted to other ML particles in the subsequent studies, including the co-doping of Nd^{3+} in $CaZnOS:Mn^{2+}$, GD^{3+} in $LiNbO_3:Pr^{3+}$, and Zr^{4+} in $SrAl_2O_4$[12, 13, 14]. In addition to co-doping, Song et al. further improved the sensitivity of $SrAl_2O_4:Eu^{2+}, Dy^{3+}$ co-doped ML particle by functionalizing it with $C_9H_{23}NO_3Si$[15]. Higher luminosity was achieved because the newly introduced chemical bonds resulted in a stronger adhesion of ML particles to the matrix, leading to a greater stress transfer to the particle. Although many studies have concentrated on enhancing the efficiency of ML particles, discovering a better composition of ML particles alone could not boost the industrial use of ML composites. This is because the full potential of the ML particle cannot be fully harnessed in the final ML composite if the production process is not optimally designed.

Therefore, the second category of research emphasizes improving the manufacturing techniques to broaden the applicability of ML composites. Recent studies have shifted from

traditional casting-based methods to employing additive manufacturing techniques for creating ML composites, leveraging their ability to construct intricate 3D shapes. Zhao et al. utilized extrusion-based 3D printing to fabricate ML composites in lattice structures, and modifying their structures enabled them to observe both isotropic and anisotropic luminescence[16]. Also, Patel et al. used PDMS doped with ML particles as building block to print soft 3D devices for pressure sensing applications[17]. Nevertheless, since the extrusion-based printing technique offers a limited printing resolution (~1mm) and requires support structures for overhangs or bridges, it is currently not the ideal method for fabricating complex 3D geometries. In addition, all the relevant studies conducted so far have been uncertain about whether the ML properties of their final products could be further enhanced, as the process parameter values were chosen in a manual manner, without a systematic framework to optimize the production process parameters[18]. All in all, developing a framework, that does not require physical insight, to optimally tune the production process parameters to fabricate high-intensity ML composites is an important hurdle to overcome.

To address these challenges, we present a novel approach where ML composite is produced via digital light processing (DLP)-based 3D printing, whose process parameters are systematically optimized through a machine learning-based optimization algorithm(**Figure 1**). DLP-based 3D printers are capable of printing intricate geometries without the need for support structures, and they are also renowned to have superior printing resolution compared to the extrusion based additive manufacturing methods that have been commonly adopted for ML composites research so far. However, the biggest hurdle in adopting DLP-based additive manufacturing to produce ML composites is that the end product's ML performance and the production time are heavily affected by the 3D printing process parameters. To address this challenge, we use multi-objective Bayesian optimization (MBO) to optimize the three salient process parameters of DLP-based additive manufacturing; material composition, layer

thickness[19], and cure depth, to achieve both strong ML properties and short printing time. As a result, the pareto-optimal process parameter solutions determined by MBO allowed us to produce the high-performance ML composites in short time. Furthermore, we validated the real-life applicability of our framework by applying the optimized DLP 3D printing method to produce the ML-based sensors and ML-base mechanical components.

2. Methodology

The ultimate objective of this research is to develop a robust additive manufacturing framework that can efficiently fabricate ML composites with various complex geometries (**Figure 1**). This framework seeks to achieve high ML intensity while also minimizing the printing time. To achieve the printing of sophisticated composites with exceptional geometric precision, here we adopt a DLP-based 3D printing method for the fabrication of ML composites (section 2.1). In our framework, we employ MBO to determine the process parameter values that leads to an outstanding balance of ML intensity and printing time, which are known to have a trade-off relationship (section 2.2). To validate the real-life applicability of the framework, we fabricate mechanoluminescent strain sensors and self-sensing mechanical components through our method and evaluate their performances (section 2.3).

2.1 Digital light processing (DLP)-based 3D printing of ML composites

DLP 3D printing is a form of additive manufacturing that uses a digital light projector to cure photopolymer resin layer by layer[20], creating highly detailed and complex objects [21, 22]. Unlike extrusion-based methods, which are commonly adopted to produce ML composites in existing studies, DLP offers superior precision and surface finish, thanks to its ability to harden an entire layer of resin simultaneously. This method achieves higher resolution because it can more accurately control the curing process down to the pixel level, enabling the production of parts with smoother surfaces and finer details.

2.1.1) Preparation of ML particle-matrix mixture

The mechanoluminescent material used in this research is rare earth-doped strontium aluminate ($SrAl_2O_4$: Eu^{2+}, Dy^{3+}), which is commonly referred to as SAOED. Here we chose the

product G-300FF (Nemoto Korea Co, South Korea) which has an average particle size of 10μm. As a matrix material, we use a translucent photopolymer produced by 3D Systems (MED AMB-10, UK) which has a tensile elastic modulus of 2.76GPa and ultimate strength of 69MPa [23]. Before the photopolymerization process, the ML particle is thoroughly mixed into the liquid state matrix, and the concentration of ML particle in the mixture is a design variable to be tuned through MBO, ranging from 5 to 30wt.%. To ensure a uniform dispersion of ML particles in the mixture, we use a planetary centrifugal mixer (MSK-300) with ceramic balls (10mm) for 15 minutes at 1000rpm. The particle agglomerates in the mixture are further decomposed by ultrasonication (VCX-750 ultrasonic liquid processor, Sonics & Materials, USA), which is performed for 120 minutes at 750W and 20kHz condition (**Figure 2.b**).

2.1.2) Printing of test samples

The ML particle-matrix mixture is hardened into a solid-state ML composite by using a DLP-based 3D printer (Figure 4 standalone, 3D Systems, USA). There are numerous process parameters in a DLP-based 3D printer that can be manipulated by the user, such as cure ratio, layer thickness, support height, light off delay. The quality and properties of the printed object are significantly influenced by how the user controls the process parameter values. Therefore, in most cases, manufacturers of the printers often also supply the materials, offering the optimal process parameter values for different materials to ensure the best outcomes. In this research, although the matrix material (MED AMB-10) is one of the materials supplied by the manufacturer (3D Systems), the process parameters suggested by the manufacturer is no longer adequate due to the dispersed ML particles in the matrix material. Therefore, we employ MBO to determine the optimal values for the two salient process parameters, cure ratio and layer thickness[19], aiming to maximize ML intensity while minimizing printing time. For the remaining process parameters, we

adhere to the recommendations provided by the manufacturer [24, 25](refer to **Table 1** in the supporting information). After the printing process, the fabricated specimen undergoes post-curing by exposure to a UV lamp (3D Systems, USA) for a duration of 8 minutes.

2.1.3) Test sample geometries and testing conditions

In this research, we employ a data-driven optimization algorithm to optimize the process parameters, aiming for increased ML intensity and reduced printing time. Here, the training data for the surrogate model is collected via real-life material printing and testing. The test specimens follow the geometrical dimensions specified in the ASTM D638 standard[26, 27]. The ML intensity of the printed tensile specimen is measured by capturing the luminescence distribution images of the tensile specimen under a uniaxial tensile deformation. To more clearly compare the ML intensities across different specimens, we increased the specimens' overall luminosity by subjecting them to ultraviolet (UV) light exposure (250–450 nm, Inno-cure 5000, LICHTZEN Co.) for a duration of one minute prior to the tensile tests (**Figure 2.a**). A universal tensile testing machine (Shimadzu AGX-V series, equipped with a 20kN load cell) is used for the tensile test, and the test is conducted in a displacement control mode at a strain rate of 0.1%/s with a data sampling rate of 100Hz. A high-resolution digital camera (Canon EOS R7, Japan, with a resolution of 32.5 megapixels) is used for the capturing of luminescence distribution images, at a sampling frequency of 30Hz. The overall setup for the measurement of ML intensity is illustrated in **Figure 2. c.**

2.2 Determination of optimal process parameters via Multi-objective Bayesian optimization.

2.2.1) Formulation of optimization problem

This study can be formulated into an optimization problem that has three independent design

variables (cure ratio r, layer thickness t, concentration of ML particle ρ), and two objective

functions (ML intensity, printing time). As discussed earlier, the three design variables are

important process parameters in the DLP-based 3D printing of ML composites that significantly

affects the two objective functions. Consequently, identifying their optimal values is critical for

building an ML composite that not only exhibits high intensity but also can be printed in short

time.

The ranges of the three design variables are set as $r = \{r \mid 2.00 \leq r \leq 5.00\}$ where r has two

decimal places, $t = \{t \mid 10\mu m \leq t \leq 100\mu m\}$ where t is an integer, and $\rho \in$

$[5wt.\%, 10wt.\%, 15wt.\%, 20wt.\%, 25wt.\%, 30wt.\%]$. Regarding the ML particle

concentration variable ρ, we consider a non-continuous design space with 6 clearly discrete levels

because the ML particle-epoxy resin mixture is manually prepared by the researcher and it

inevitably introduces a random error, although typically minor. Among our two objective

functions, the ML intensity is measured via material printing and testing method elaborated in

section 2.1.2. To quantify the ML intensity, we compute the 'intensity per pixel' value inside our

region of interest (test specimen), based on the images taken during the tensile test. For measuring

the printing time, we use the total time elapsed for the printing, which is shown on the DLP

printer's display.

2.2.2) Multi-objective Bayesian optimization

Bayesian optimization is a data-driven strategy to sequentially explore a design space,

aiming to identify the global optimum in a data-efficient way, especially when the objective

function is not defined in a functional form. This optimization framework approach proves highly

beneficial when the collection of a large dataset is difficult due to the objective function being

expensive-to-evaluate, and the optimization problem has a small number of input variables.

Figure. 3 illustrates the complete optimization process in a schematic flowchart.

In this research, we use Gaussian process regression (GPR) as a surrogate model, which is the most commonly used regression model for Bayesian optimization. GPR is a statistic regression model that can model the complex input-output relationship $y = f(\mathbf{x}) + \varepsilon$ by interpolating the given set of observation data $\mathcal{D} = \{(\mathbf{x_i}, y_i)|i = 1, \dots, n\}$. The noise variance of the prediction $\varepsilon \sim N(0, \sigma_\varepsilon^2)$ is assumed to have Gaussian distribution. GPR model predicts the objective function value $f(\mathbf{x}^*)$ at an unknown input feature $\mathbf{x}^*$ by assuming that the training data (observation data) points $\mathbf{y} = \{y_i|i = 1, \dots, n\}$ and the new prediction $y^* = f(\mathbf{x}^*)$ are correlated by multivariate Gaussian distribution:

$$P_{y,y^*} = \begin{bmatrix} \mathbf{y} \\ y^* \end{bmatrix} \sim N\left(0, \begin{bmatrix} \mathbf{K} & \mathbf{k} \\ \mathbf{k}^T & k(\mathbf{x}^*, \mathbf{x}^*) \end{bmatrix}\right)$$

Where $\mathbf{K} = K_{ij} = k(\mathbf{x}_i, \mathbf{x}_j)$ is a covariance matrix and $\mathbf{k} = k_i = k(\mathbf{x}_i, \mathbf{x}^*)$ is a covariance vector whose elements are computed by a covariance function $k(\mathbf{x}_i, \mathbf{x}_j)$, which quantifies the joint variability of different outputs. In this research, we utilized Matern 5/2 function as our covariance function.

$$k(\mathbf{x}_i, \mathbf{x}_j) = \sigma_f^2 \left(1 + \frac{\sqrt{5}r}{l} + \frac{5r^2}{3l^2}\right) exp\left(-\frac{\sqrt{5}r}{l}\right) + \delta_{ij}\sigma_\epsilon^2$$

where

$$r = \sqrt{(\mathbf{x}_i - \mathbf{x}_j)^T(\mathbf{x}_i - \mathbf{x}_j)}$$

and δ_{ij} is a Kronecker delta function. σ_f^2, l, σ_ϵ^2 are the hyperparameters that has to be tuned by the user. To determine the optimal set of values for the hyperparameters, we use maximum likelihood estimation (MLE) scheme[28, 29]. In this study, a Markov chain Monte Carlo (MCMC)-based

Bayesian inference is employed to determine the optimal set of hyperparameters that results in the maximum likelihood.

To prepare the initial training dataset for our initial GPR model, 12 distinct input combinations are chosen within the process parameter design space. To uniformly allocate the 12 initial data collection points within the three-dimensional design space, we use Latin hypercube sampling method. Then, the objective function values of the 12 different input combinations are evaluated.

Using the initial training data set, we train our initial GPR model. A Python-based open-source Gaussian process library 'GPy' developed by the Sheffield machine learning group is used to conduct the computations related to the GPR. An important matter to consider in this study is that the cure ratio and layer thickness are 'continuous' design variables, while the ML particle concentration is rather a 'non-continuous' design variable as it consists of only 6 discrete levels. To effectively handle our design space, which encompasses both continuous and discrete design variables, we customized the GPy library by implementing a special GPR model recently developed by Park et al, which is capable of modeling both variable types[28]. The trained surrogate model allows for the probabilistic prediction of objective function values at unknown design points.

Then, the trained GPR model is used for the Bayesian optimization. Bayesian optimization is a repetitive optimization scheme, which uses the trained surrogate model to propose a new query point in the design space, and then updates the surrogate model by appending this newly acquired data to the training set. Bayesian optimization allows us to explore the design space in a data-efficient manner by repeatedly sampling a new data point at the location that has the maximum value of 'acquisition function'. There exist multiple types of acquisition function, yet they are all

aimed at strategically suggesting a new input design that not only tries to reach the best objective function value (exploitation), but also tries to improve the GPR model's predictive capability (exploration). Since our goal is to enhance multiple objective functions simultaneously, we choose Expected Hypervolume Improvement (EHVI) as our acquisition function, which is commonly adopted for Multi-objective Bayesian optimization[28, 30].

Starting with the GPR model trained with 12 initial training data, we performed 6 repetitions of MBO sampling in order to determine the pareto-optimal sets of input variable values that allow us to print a high intensity ML composite in a short time.

2.3 Validation of the framework: 3D printing of ML composites for practical application

To validate the real-life applicability of the proposed additive manufacturing framework, we fabricate two potential applications of ML composites in the future industries using the optimal process parameters determined through MBO. For one, we use the framework to fabricate mechanoluminescent stress sensors having complex geometries (section 2.3.1). In addition, we produce mechanoluminescence-based self-sensing mechanical components, demonstrating how our framework can advance mechanoluminescent composites into the forefront of next-generation structural health monitoring (section 2.3.2).

2.3.1) Mechanoluminescent stress sensors

Before fabricating complex three-dimensional sensors, we begin by printing a two-dimensional sensor with a honeycomb shape.[31, 32]. This initial step helps us confirm that our printed ML product has the ability to transduce mechanical stress into visible light. We employ ABAQUS simulation to compute the stress field within the two-dimensional honeycomb structure when subjected to an external load in lateral direction. Then, we print the identical structure using

ML composite and conduct the same tensile test in real life. This allows us to examine if the intensity of the emitted light correlates directly with the stress field computed from the simulation. After the validation with a simple 2D example, we proceed to print a patch-like stress sensor structure that readily attaches to three-dimensional curved surfaces[33] , as well as a cylindrical stress sensor structure (**Figure 1**). This is done to determine if the ML composite stress sensors can visually represent their stress field through emitted light. Both 3D sensor structures were modeled with Solidworks.

2.3.2) Mechanoluminescence-based Self-sensing mechanical components

To validate the applicability of 3D printed ML-composites to structural health monitoring, we used the ML-composites to print commonly used mechanical components, such as a bolt and nut[34 -36]. The geometric dimensions of these components adhere to the M10 thread dimension standard, and the printing of these structures uses optimized process parameters obtained from MBO. To examine their mechanoluminescent response to shear stress, we devised a special tensile test setup. The tensile test is conducted in a displacement control mode at a strain rate of 0.1%/s with a data sampling rate of 100Hz.

3. Results and Discussion

3.1 Digital light processing (DLP)-based 3D printing of ML composites

In this research, DLP-based 3D printing is employed for the fabrication of ML composites in complex geometries. To evaluate how well the DLP-based 3D printing method works for producing ML composites, we performed FTIR spectra analysis[37] and SEM image analysis on the ML composite samples produced by this method. **Figure 4.a** illustrates the FTIR spectrum of the ML composite (epoxy resin doped with ML particles) produced using our proposed method, alongside the FTIR spectrum of the pristine epoxy resin. At lower wavenumbers, the FTIR spectrum of the ML composite shows distinct peaks at 645 cm^{-1}, 780 cm^{-1}, and 850 cm^{-1}, suggesting that SAOED ML particles are successfully incorporated in the epoxy resin. Above 1000 cm^{-1}, the spectrum of the ML composite aligns with that of the pristine resin. This comparative analysis of the FTIR spectra reveals that the photopolymerization process used in DLP-based 3D printing did not result in any undesired changes in chemical composition, ensuring that both the ML particles and the epoxy resin maintain their separate existences in the final product.

Figure 4.b and **Figure 4.c** are the SEM images of pristine epoxy resin product while **Figure 4.d** and **Figure 4.e** are the SEM images of ML composite captured in different magnifications. From the SEM images taken from ML composite, it could be observed that our method to prepare the liquid state mixture of ML particle and epoxy resin can effectively form a uniform suspension of ML particles in the epoxy resin, and the DLP-based 3D printing process did not cause any re-agglomeration of the ML particles during the hardening. It's crucial for the particles to be well distributed in the composite as this enhances mechanical properties by reducing stress concentration and improves ML intensity by ensuring better attachment to the matrix. In addition, the layer-by-layer integrity observed in **Figure 4.d**, which is almost as good as that seen from

Figure 4.b, allows us to understand that the DLP-based photopolymerization process could sufficiently form a strong bonding of printing layers despite the presence of ML particles in the epoxy resin.

To examine the printed ML composite's ability to transduce the mechanical stress into visible light, we used the method elaborated in section '2.1.3) Test sample geometries and testing conditions' to print a dog bone specimen and perform a uniaxial tensile test while measuring the light emission. From the result shown in **Figure 5**, we could observe that the intensity of emitted light is directly proportional to the level of tensile load exerted onto the test sample. In addition, the images of the ML composite specimen captured at different stages of deformation (i, ii, iii, iv) demonstrate that the light emitted enables direct monitoring of the stress field within the material. During the initial phases of deformation (i, ii), the light emission uniformly and gradually intensifies across the entire specimen, indicating that the specimen is undergoing homogeneous elastic deformation. Subsequently, there is a significant increase in light emission from a small area experiencing stress concentration (iii), followed by complete failure of the sample due to the onset of brittle crack propagation in the same region (iv). This result, once again, underscores the significant potential of ML composite as an advanced technique for structural health monitoring in the future.

3.2 Determination of optimal process parameters via Multi-objective Bayesian optimization

3.2.1) Acquisition of initial training data and training of initial GPR

For the collection of initial training data, uniform Latin hypercube sampling was conducted to define 12 uniformly distributed data acquisition points within the design space. As a result,

initial query points are defined as shown in **Table 1**. To measure the objective function values (ML intensity, printing time) for these initial query points, samples were fabricated using the corresponding process parameters and then subjected to tensile testing. The resultant objective function values are shown in **Table 1**, and they are graphically illustrated in the **Figure 6.a**.

Using these initial data sets, the initial Gaussian Process Regression (GPR) model was trained. As a result of conducting Hamiltonian Monte Carlo (HMC) based Markov Chain Monte Carlo (MCMC) sampling, optimal set of hyperparameter values that maximizes the likelihood function were identified. Training the initial GPR with the optimal hyperparameters and initial training data yielded the initial GPR model, as shown on the left-hand side of **Figure 7.a** and **Figure 7.b** (MBO iteration: 0). Since the GPR model in this study has three input variables, it is impossible to graphically illustrate the GPR model. Therefore, in **Figure 7.a**, we plotted a 'cross section' of the trained GPR model by fixing the cure ratio (r) and concentration of ML particle (ρ) to 2.00 and 30wt.%, respectively. In **Figure 7.b**, we plotted the heat map of the GPR model for ML intensity by fixing the cure ratio (r) to 2.00, where the upper plots represent the predicted mean value of ML intensity, and the lower plots represent the prediction variance. As it can be observed from the figures, GPR model not just provides a reasonable prediction of objective function at unexplored input designs (blue solid lines in **Figure 7.a** and upper contour plots in **Figure 7.b)**, but it also tells us the uncertainty of the prediction made (light blue shaded area in **Figure 7.a** and lower contour plots in **Figure 7.b).** It is worth noting that the GPR contour plots in **Figure 7.b** has discrete characteristic along the y-axis, because the concentration (ρ) is a non-continuous design variable. Such characteristics noted in the figures emphasize the successful implementation of the discrete GPR model which we elaborated in section '**2.2.2) Multi-objective Bayesian optimization**'.

3.2.2) Multi-objective Bayesian optimization cycles

The trained GPR model is used for the first cycle of MBO. Leveraging the predictive power of the trained GPR model, the input configuration with the highest Expected Hypervolume Improvement (EHVI) function value was derived as the next query point, which was (r, t, ρ)=(2.00, 51μm, 30wt.%). Our initial GPR model's prediction at this new query point can be seen from the plots named 'MBO iteration: 0' in Figure 6.a). As it can be observed from the plots, this new query point is predicted to have high objective function values, and at the same time, the GPR model currently has high prediction uncertainty around this region. This indicates that our new query point is a suitable point for adding a new observation data, in terms of both exploitation (searching for a design that is expected to have high objective function) and exploration (enhancing the GPR model by adding a new data point at a location where the surrogate model has high prediction variance).

Using the same method that was employed to acquire the initial data, the objective function values for this new query point were measured, yielding a ML intensity of 0.222 and a printing time of 132 s. Then, a new GPR model was trained based on a total of 13 observation data, including this new data. The updated GPR model is shown in the plot named 'MBO iteration: 1' in Figure 6, from which we can note a reduction in prediction uncertainty in region near the newly added data point. By repeating this MBO cycles 6 times, we obtained 6 new sets of process parameters suggested by MBO. As it can be seen from both Table n and Figure 7.a, the pareto-optimal process parameter sets suggested by MBO have superior balance of ML intensity and printing time compared to the initial training data. Furthermore, it can be noted from Figure 6 that the GPR model's prediction uncertainty continuously decreases with each iteration of the MBO cycles.

The result reveals the power of using MBO for the optimization problems that have objective functions that are highly expensive to evaluate, just like our case where we had to employ 3D printing of specimens and tensile tests to evaluate the objective functions. The MBO algorithm utilizes GPR as a surrogate model, which optimally utilizes each observation data point to make predictions (since it takes into account the covariance between all combinations of observation data to make a prediction at an unexplored design), and carefully selects a new query point by considering both *exploitation* and *exploration*. Consequently, the MBO algorithm enabled us to identify multiple sets of pareto-optimal process parameters that results in an excellent balance of ML intensity and printing time, with fewer than 10 data samples. During the early stage of optimization, the algorithm selected input designs whose objective function values were marginally higher than the initial 12 designs. As optimization progressed, the process parameters moved towards the region of high performance that is not dominated in the output space.

To verify whether employing the identified pareto-optimal process parameters can produce ML composites with precise 3D geometrical features (in a scale of hundreds of micrometers), we printed two complex shapes (a 2D rectangular plane with cavities and a 3D rectangular block with conical extrusions) using one of the pareto-optimal process parameters determined from MBO: $(r, t, \rho) = $ **(2.6, 42μm, 30%)**. We then compared the dimensions of the printed items to the initially intended geometrical specifications (**Figure 6.b**). The results revealed that the 3D printing process parameters identified through MBO can produce the ML composites in complex shapes with a high degree of geometric accuracy (with marginal level of error).

3.2.3) Physical understanding of the input-output relationship

Adopting MBO for the optimization of 3D printing process is intriguing because it not

only generates the pareto-optimal solutions, but the generated solutions help us to empirically understand the complex non-linear relationship between the inputs and outputs. To grasp the physics behind the input-output relationship, we thoroughly analyze the observation data and capture the 'general trend' of how each of the input variables (r,t,ρ) affects the two objective functions (**Figure 6.a**).

Cure ratio (r)*: Upon examining the distribution of observation data in the output space, it seems there is a notable correlation between cure ratio and printing time, while the relationship between cure ratio and ML intensity appears to be weak. Although there are exceptions, it is generally observed that data points with high printing time scores tend to have a low cure ratio, approximately around 2. This suggests that a lower cure ratio significantly benefits the reduction of printing time. On the other hand, regarding the effect of cure ratio on ML intensity, the pareto optimal design solution that led to highest intensity score had a cure ratio of 2.6. This allowed us to understand that it is important to avoid the over-curing or under-curing of printed layers by pinpointing the optimal cure ratio value, which is neither too high nor too low.

To understand the effect of over-curing and under-curing on the printed product's ML intensity, we printed the tensile specimens with 3 different cure ratio values 2.0 (under-curing), 2.6 (optimal), and 4.9 (over-cured), and compared their mechanical and mechanoluminescent performance (**Figure 8**). The experimental results reveal that choosing an optimal cure ratio value allows the printed product to have superior mechanical and ML performance (**Figure 8.a and Figure 8.b**). The SEM image of the over-cured sample (**Figure 8.c**) show that it has relatively weak integration between the printed layers, which may result in inhomogeneous stress distribution within the structure which is detrimental in terms of both mechanical and ML property. On the other hand, the SEM image of optimally cured sample exhibits a homogeneous

microstructure, which allows the overall structure to function as more efficient load bearing medium and better mechanoluminescent transducer.

All in all, reducing the cure ratio provides significant benefits in printing time, while there is an optimal cure ratio level ($r = 2.6$) that benefits the ML intensity. Therefore, it is important that the user carefully select the cure ratio value observed in the Pareto front, depending on which objective function the user wants to focus better on.

Layer thickness (t)*:* From **Figure 6.a**, a clear correlation can be noted between layer thickness and printing time. Increasing the layer thickness means that thicker layers can be printed within the same timeframe, which consequently allows the final product to be printed in shorter time. In contrast to the cure ratio *(r)*, which showed marginal correlation with ML intensity, layer thickness exhibits a significant correlation with ML intensity. Although there are some exceptions, data showing high ML intensity typically feature lower layer thicknesses. This is because reducing layer thickness enables more thorough photopolymerization for each printing layers, resulting in better cohesion between the ML particles and the epoxy resin matrix. Therefore, layer thickness can serve as a crucial parameter that controls the balance between ML intensity and printing time. The way users adjust this variable allows them to prioritize one objective function over another, aligning with their particular requirements.

ML particle concentration (ρ)*:* Upon examining the distribution of observation data in the output space, it seems there is a notable correlation between ML particle concentration and ML intensity, while the relationship between ML particle concentration and printing time appears to be weak. Although there are exceptions, it is generally observed that data points with high ML intensity scores tend to have a high ML particle content, usually above 15wt.%[15]. This suggests that a higher ML particle content significantly benefits the printed product's ML intensity. On the other

hand, considering that the variance of data along the y-axis seems nearly random in terms of ML particle concentration, this process parameter appears to have only a marginal effect on the printing time, as expected. Therefore, as increasing the ML particle concentration does not increase the printing time while providing significant benefits in ML intensity, most pareto-optimal designs are observed to have ML particle concentration over 15wt.%. Although this trend may be true in general sense, there are exceptions depending on the values of other input variables. Therefore, it cannot be conclusively stated that increasing the ML particle concentration is 'always' advantageous. As the concentration of ML particles increases, a delicate trade-off between improved dispersion and enhanced stress transfer emerges, influenced by the cure ratio and layer thickness.

All in all, as a general guideline, we could conclude that if one's target is to print a ML composite for high ML intensity in short printing time, it is important that he reduces the cure ratio (r) and try to avoid the ML particle content (ρ) lower than 15wt.%. To control the balance between the two objective functions (prioritize one objective function over another), one can adjust the cure ratio (r) and layer thickness (t) based on the trends that can be observed from the pareto-optimal solutions determined by MBO.

3.3 Validation of the framework: 3D printing of ML composites for practical application

In this research, we proposed a novel additive manufacturing process for the fabrication of ML composites, where we use DLP-based 3D printing technique whose key process parameters are optimized via Multi-objective Bayesian optimization. To validate the real-life applicability of the proposed framework, we fabricated two potential applications of ML composites in the future

industries using one of the pareto-optimal process parameter sets determined through MBO: $(r, t, \rho) = (2.6, 42\mu m, 30\%)$ which resulted in an excellent balance of ML intensity and printing time.

3.3.1) Mechanoluminescent stress sensors

Before producing complex three-dimensional sensors, we created a simple two-dimensional sensor with a honeycomb pattern to test whether the ML composite formed using our framework could effectively convert mechanical stress into visible light. As depicted in **Figure 9.a,** the stress field in the sensor under external tensile load, computed through material simulation, and the ML intensity field obtained from the real experiment show qualitatively matching trend. In addition, the graphs in **Figure 9.b** showing the distribution of von-Mises stress and ML intensity along the tensile direction suggest that the ML composite sensor produced using our framework can effectively display its real-time stress field through visible light. Furthermore, **Figure 9.c** helps us to understand that the change of external load and light intensity during the sensor's deformation process are quite comparable.

Having confirmed that the ML composites produced using our framework effectively operate as stress-light converters, we employed our framework to create a patch-like stress sensor design that can easily adhere to three-dimensional curved surfaces, as well as a cylindrical stress sensor structure that has excellent strength-to-weight ratio against compressive load (**Figure 9.d**). The change in light intensity observed during the elastic deformation of the sensors under external forces indicated that the sensors were capable of operating effectively in a reversible manner. Thanks to the highly precise 'lattice' geometry and three-dimensional curvature that could be achieved with our DLP-based 3D-printing framework, the sensors not only offer excellent geometric adaptability tailored to their specific purpose, but also possess a high elastic strain range,

allowing for a wide sensing range without any hysteresis.

3.3.2) Mechanoluminescence-based Self-sensing mechanical components

To confirm the suitability of 3D printed ML-composites for structural health monitoring applications, we utilized our framework to fabricate mechanical components based on ML composites, a bolt-nut connection system (**Figure 10**). The DLP-based printing framework could print the bolts and nuts with highly precise and accurate dimensions for screw threads, ensuring that they fit together smoothly upon assembly. As depicted in **Figure 10.a**, the bolt-nut assembly demonstrated a remarkable mechanoluminescent reaction when subjected to increasing shear stress. Moreover, the light intensity video captured during the deformation process enabled us to pinpoint the location of stress concentration (evidenced by the sharp peak in the graph in **Figure 10.b**), which threatens the structural health of the mechanical component. The result shows how our framework can advance mechanoluminescent composites to the forefront of next-generation structural health monitoring.

4. Conclusion

In this research, we presented a novel approach where $SrAl_2O_4{:}Eu^{2+}, Dy^{3+}$ particle-based mechanoluminescent composite can be produced in complex 3D shapes via digital light processing (DLP)-based 3D printing, whose process parameters are optimized through a machine learning-based optimization algorithm. We adopted multi-objective Bayesian optimization to optimize the three salient process parameters of DLP-based additive manufacturing; ML particle content, layer thickness, and cure ratio, to achieve both strong ML properties and short printing time. Gaussian process regression is used for the modeling of complex input-output relationship, and the training data is collected by performing actual experiments. As a result, the pareto-optimal process parameter solutions determined by 6 cycles of MBO allowed us to produce the ML composites that have high ML intensity in short printing time. Also, the optimized process parameters allowed us to print the ML composite into complex 3D shapes, with much higher printing precision and accuracy compared to the common extrusion-based ML composite 3D printing processes. Another fascinating fact about adopting MBO for the designing of 3D printing process parameters was that the pareto-optimal solutions generated by MBO allowed us to empirically understand how the process parameters affect the end product's ML property and the overall printing time. Finally, we validated the real-life applicability of our framework by applying the optimized DLP-based 3D printing framework to produce and test the ML-based sensors and ML-based mechanical components.
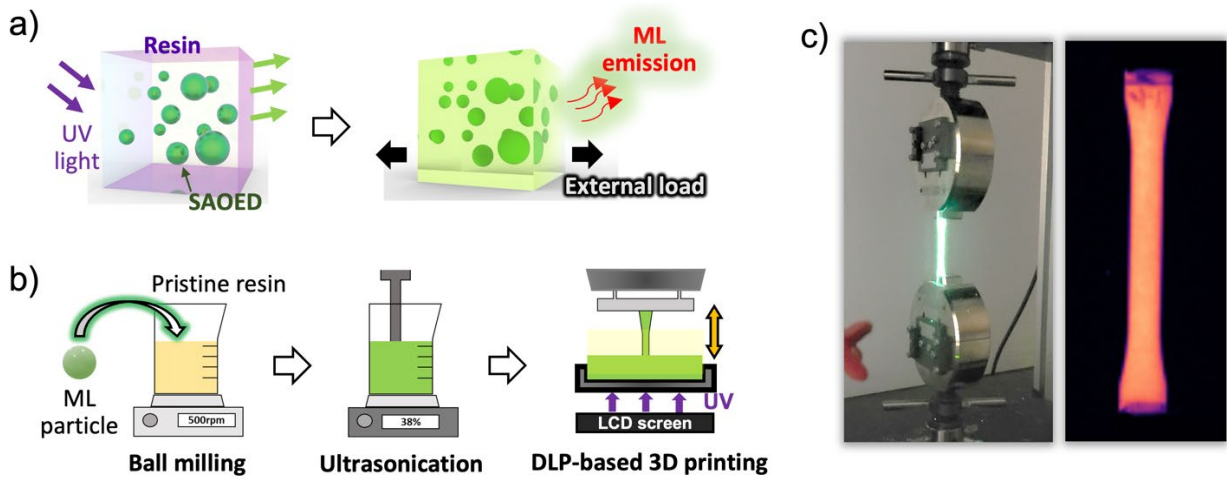
Figures & Tables
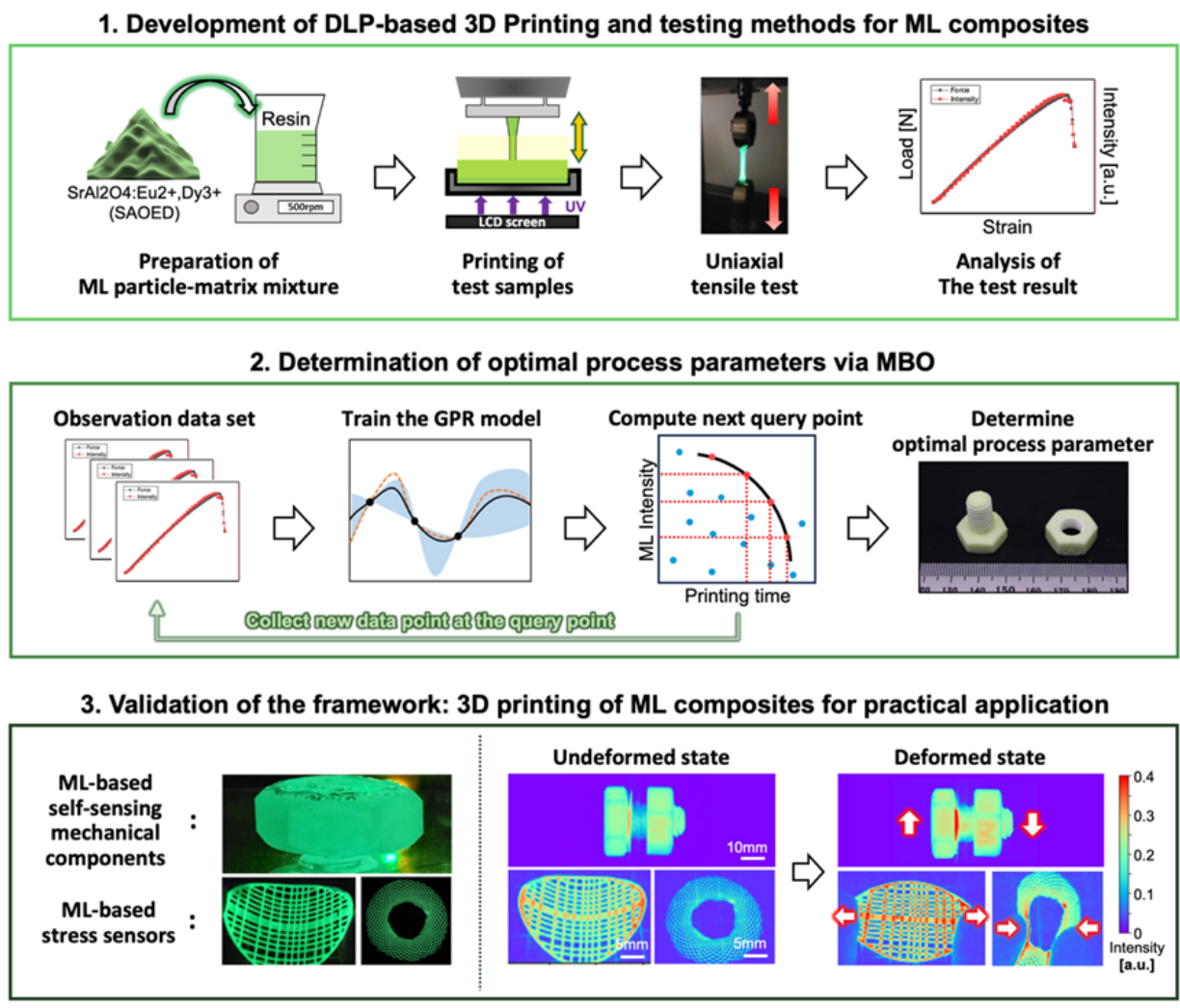
Figure 1. Schematic diagram of key milestones for the development of DLP-based 3D printing framework for ML composites.

Figure 2. Key mechanisms and procedures involved in the fabrication of ML composites through DLP-based 3D printing. (a) Schematic diagram of mechanoluminescence emission mechanism activated by UV charging. (b) Schematic diagram of ML composite synthesis and hardening. (c) The tensile test conducted for the evaluation of ML intensity.
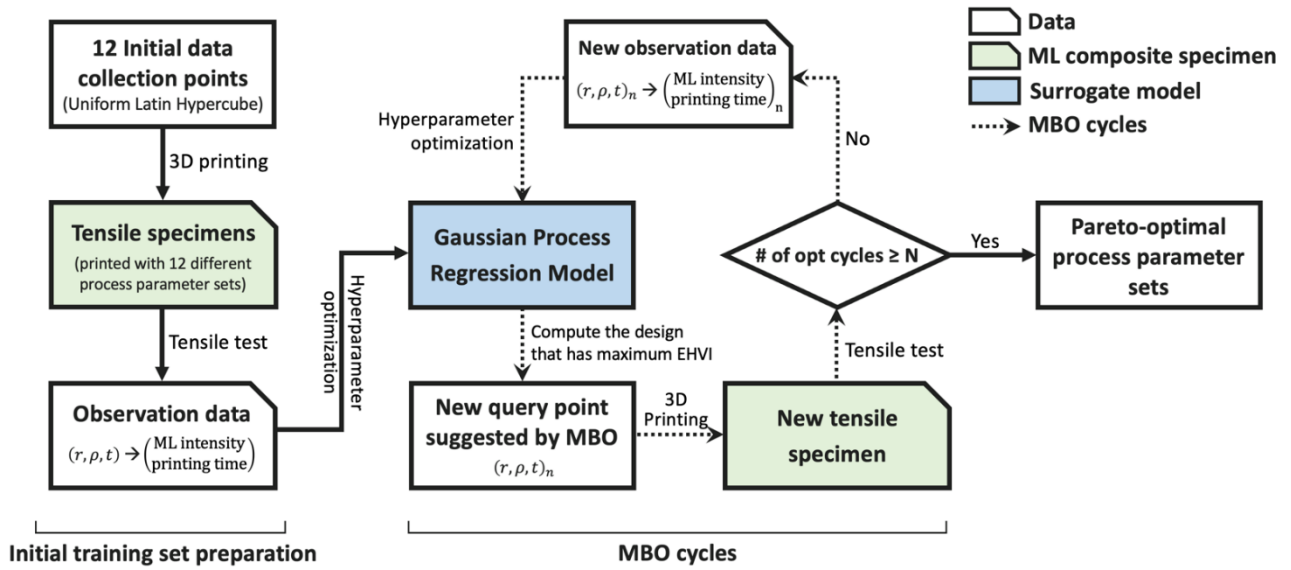
Figure 3. Overall workflow chart of Multi-objective Bayesian optimization (MBO) for the determination of pareto-optimal process parameters
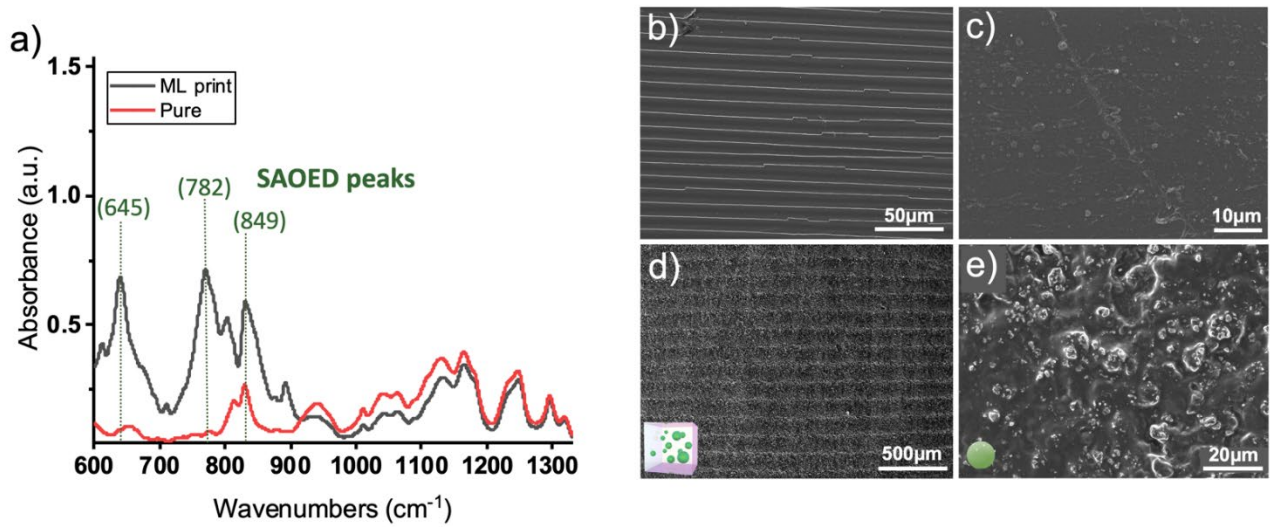
Figure 4. Post processing conducted on the ML composite sample produced via DLP-based 3D printing. (a) FTIR spectrum analysis for 3D printed pure matrix (epoxy resin polymer) and ML composite. (b, c) SEM images of 3D printed pure matrix. (d, e) SEM images of 3D printed ML composite at different magnification ratios.
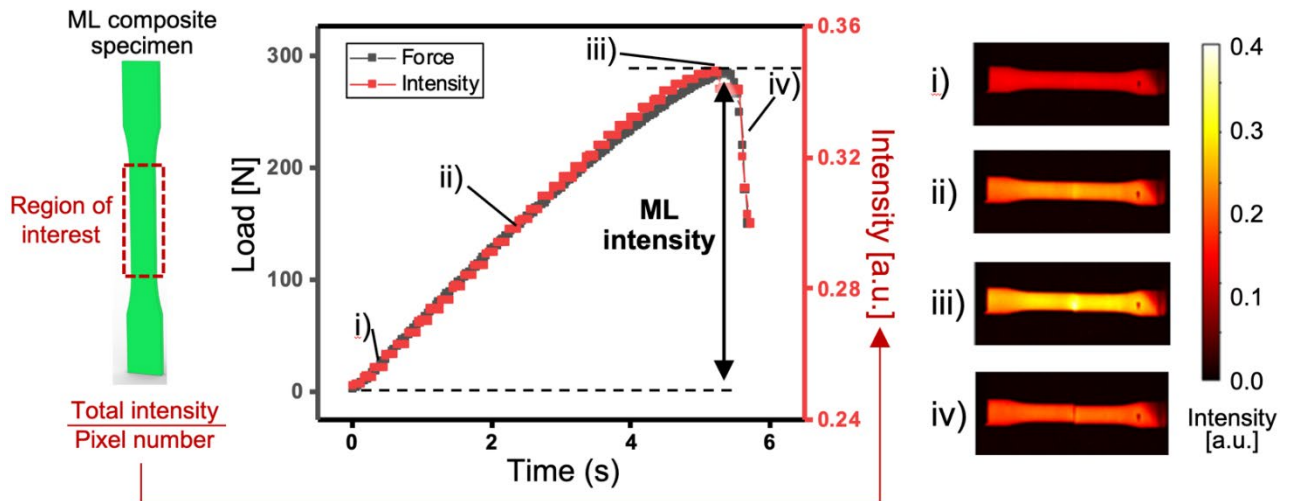
Figure 5. Analysis of correlation between exerted external load and intensity of emitted light of ML composite specimen during the uniaxial tensile test.
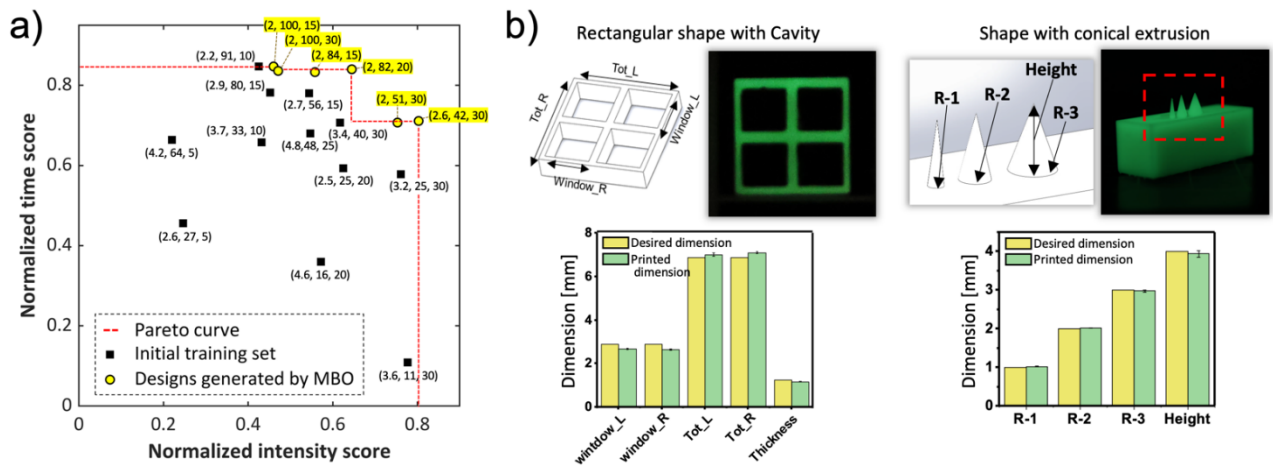
Figure 6. The result of MBO. (a) The training data and MBO generated data are scattered on the objective function grid. (b) Excellent geometrical precision observed from the ML composite structures that are printed with pareto-optimal process parameters determined by MBO.
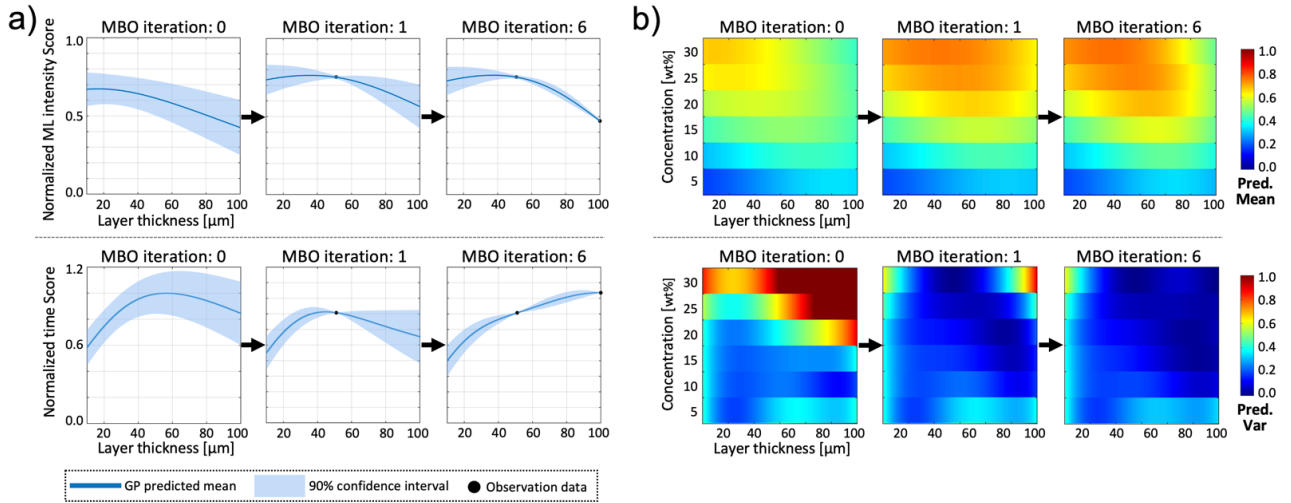
Figure 7. Variation in the Gaussian process regression model across Bayesian optimization cycles. (a) Cross-sectional view of the GPR model along the layer thickness t, with the other two design variables held constant at $r = 2.00$ and $\rho = 30\%$. The GPR models for predicting ML intensity are displayed above, and those for predicting printing time are shown below. (b) Heat-map visualization of the GPR model for predicting ML intensity with r held constant at 2.00. GPR prediction mean are displayed above and GPR prediction variance are shown below.
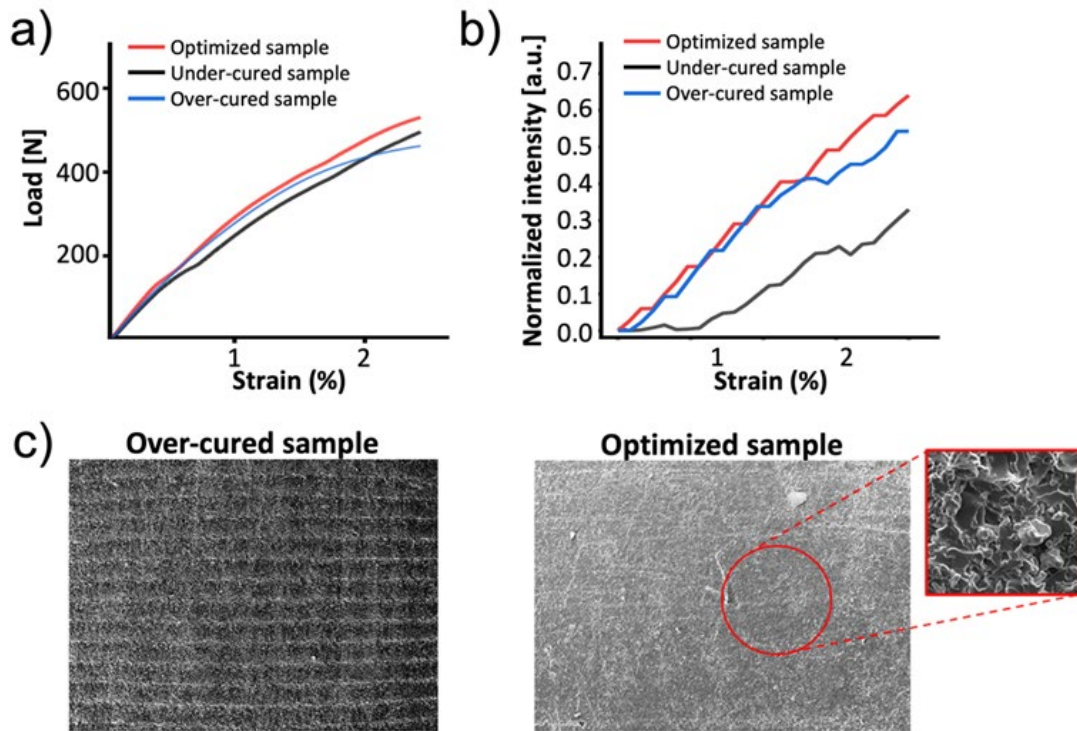
Figure 8. Effect of cure ratio variable *r* on the mechanical and mechanoluminescent properties of printed product. (a) Load-strain graphs and (b) ML intensity-strain graphs of ML composite specimens printed with different cure ratio. (c) SEM images of ML composites printed with high cure ratio and optimal cure ratio.
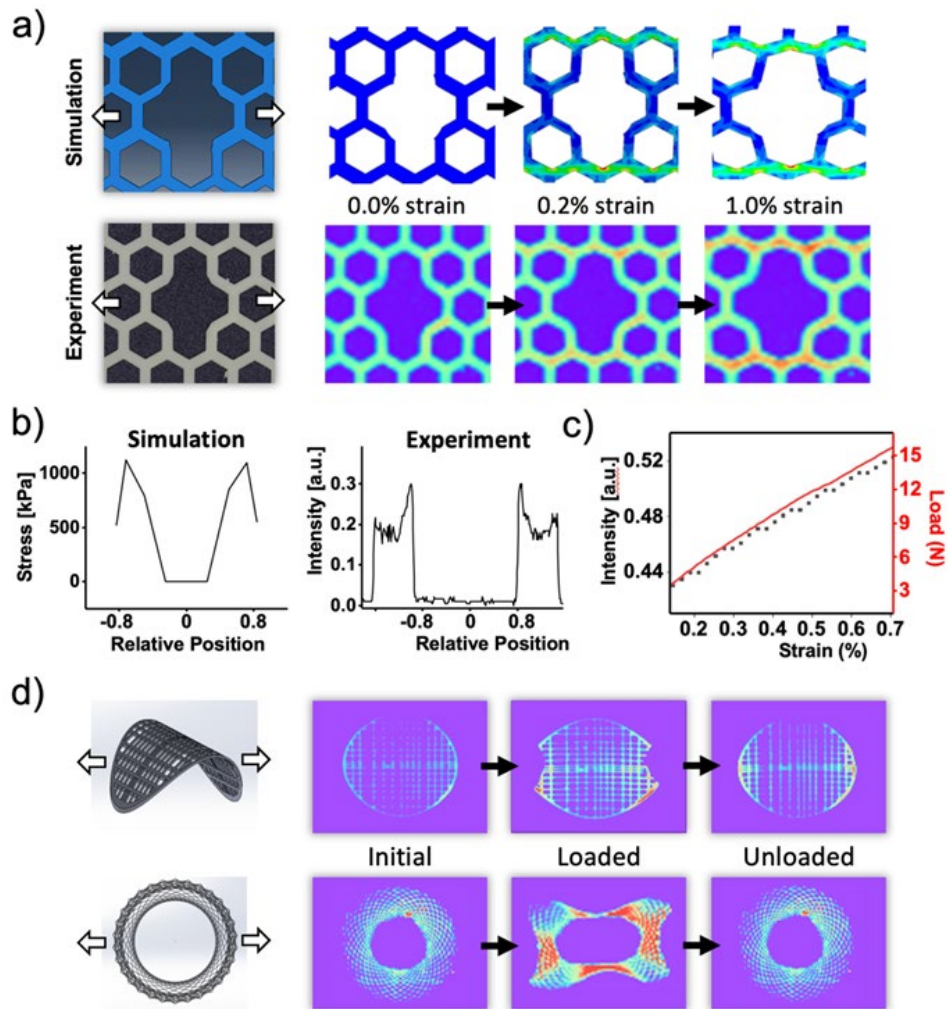
Figure 9. Mechanoluminescent stress sensors printed with our framework. (a) Mechanoluminescent property observed from a simple two-dimensional sensor with a honeycomb pattern. (b) Distribution of von-Mises stress and ML intensity along the tensile direction. (c) The change in external load and light intensity during the sensor's deformation process. (d) A 3-dimensional patch-like stress sensor and a cylindrical stress sensor structures printed with DLP-based 3D printing.
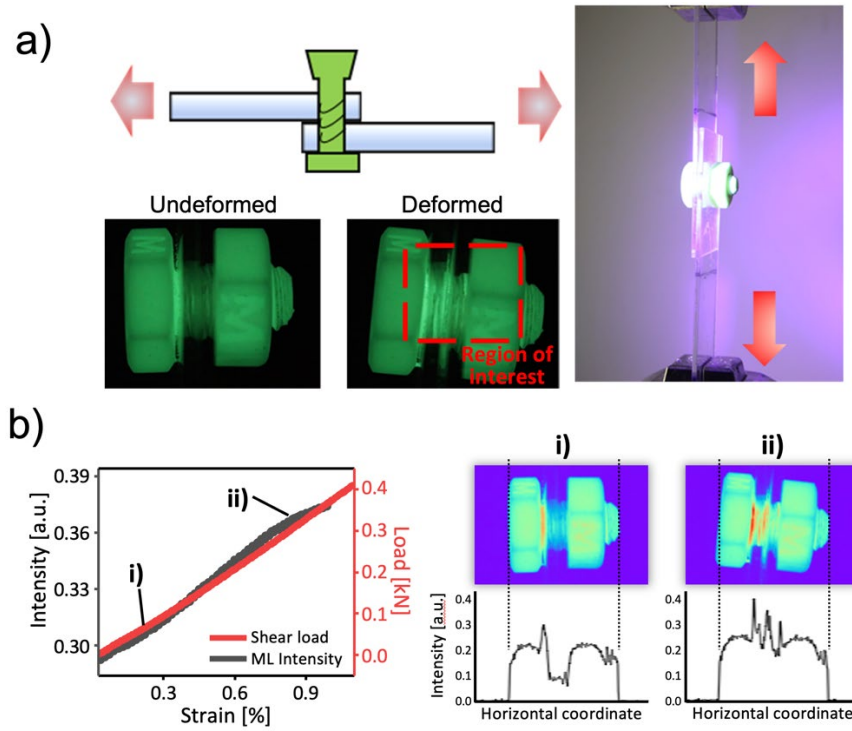
Figure 10. Mechanoluminescence-based self-sensing mechanical components. (a) Setup of the tensile test to exert shear load on the mechanical component. (b) Mechanoluminescent property allows us to monitor the increase in stress within the mechanical components.

Table

#	Cure ratio r	Layer thickness t [μm]	Concentration ρ [%]	ML intensity [a.u.]	Printing time [min]
1	4.8	48	25	0.161	144
2	2.9	80	15	0.143	98
3	4.6	16	20	0.173	288
4	2.2	91	10	0.132	69
5	3.4	40	30	0.191	132
6	3.7	33	10	0.133	154
7	2.7	56	15	0.161	99
8	2.5	25	20	0.182	183
9	3.2	25	30	0.232	190
10	4.2	64	5	0.063	151
11	2.6	27	5	0.072	245
12	3.6	11	30	0.231	401
MBO 1	2	51	30	0.222	132
MBO 2	2.6	42	30	0.243	120
MBO 3	2	82	20	0.191	72
MBO 4	2	100	15	0.142	69
MBO 5	2	84	15	0.167	75
MBO 6	2	50	20	0.141	74

Table 1. Training data and MBO generated data

References

[1]   A. D. B. L. Ferreira, P. R. O. Nóvoa, and A. T. Marques, 'Multifunctional Material Systems: A state-of-the-art review', *Compos Struct*, vol. 151, pp. 3–35, 2016, doi: 10.1016/j.compstruct.2016.01.028.

[2]   J. Narayana and R. Gupta Burela, 'A review of recent research on multifunctional composite materials and structures with their applications', 2018. [Online]. Available: www.sciencedirect.comwww.materialstoday.com/proceedings

[3]   C. Wang, D. Peng, and C. Pan, 'Mechanoluminescence materials for advanced artificial skin', *Science Bulletin*, vol. 65, no. 14. Elsevier B.V., pp. 1147–1149, Jul. 30, 2020. doi: 10.1016/j.scib.2020.03.034.

[4]   Y. Zhuang and R. J. Xie, 'Mechanoluminescence Rebrightening the Prospects of Stress Sensing: A Review', *Advanced Materials*, vol. 33, no. 50. John Wiley and Sons Inc, Dec. 01, 2021. doi: 10.1002/adma.202005925.

[5]   J. Liu *et al.*, 'A multifunctional composite material with piezoresistivity and mechanoluminescence properties for a wearable sensor', *Compos Sci Technol*, vol. 236, May 2023, doi: 10.1016/j.compscitech.2023.109993.

[6]   Z. Guo and W. Chen, 'Using mechanoluminescence as a low-cost, non-destructive diagnostic method for transient polymer impact processes', *Measurement (Lond)*, vol. 151, Feb. 2020, doi: 10.1016/j.measurement.2019.107173.

[7]   Y. Fujio, C. N. Xu, Y. Sakata, N. Ueno, and N. Terasaki, 'Invisible crack visualization and depth analysis by mechanoluminescence film', *J Alloys Compd*, vol. 832, Aug. 2020, doi: 10.1016/j.jallcom.2020.154900.

[8]   S. Timilsina, J. S. Kim, J. Kim, and G. W. Kim, 'Review of state-of-the-art sensor applications using mechanoluminescence microparticles', *International Journal of*

Precision Engineering and Manufacturing, vol. 17, no. 9, pp. 1237–1247, Sep. 2016, doi: 10.1007/s12541-016-0149-y.

[9]   X. Wang *et al.*, 'Dynamic pressure mapping of personalized handwriting by a flexible sensor matrix based on the mechanoluminescence process', *Advanced Materials*, vol. 27, no. 14, pp. 2324–2331, Apr. 2015, doi: 10.1002/adma.201405826.

[10] A. Feng and P. F. Smet, 'A review of mechanoluminescence in inorganic solids: Compounds, mechanisms, models and applications', *Materials*, vol. 11, no. 4. MDPI AG, Mar. 23, 2018. doi: 10.3390/ma11040484.

[11] H. Zhang, H. Yamada, N. Terasaki, and C. N. Xu, 'Ultraviolet mechanoluminescence from SrAl2O4:Ce and SrAl2O4:Ce,Ho', *Appl Phys Lett*, vol. 91, no. 8, 2007, doi: 10.1063/1.2772768.

[12] M. Su *et al.*, 'Largely enhanced elastico-mechanoluminescence of CaZnOS: Mn2+ by co-doping with Nd3+ ions', *J Lumin*, vol. 217, Jan. 2020, doi: 10.1016/j.jlumin.2019.116777.

[13] G. Qiu, H. Fang, X. Wang, and Y. Li, 'Largely enhanced mechanoluminescence properties in Pr3+/Gd3+ co-doped LiNbO3 phosphors', *Ceram Int*, vol. 44, no. 13, pp. 15411–15417, Sep. 2018, doi: 10.1016/j.ceramint.2018.05.193.

[14] L. Liu, C. N. Xu, A. Yoshida, D. Tu, N. Ueno, and S. Kainuma, 'Scalable Elasticoluminescent Strain Sensor for Precise Dynamic Stress Imaging and Onsite Infrastructure Diagnosis', *Adv Mater Technol*, vol. 4, no. 1, Jan. 2019, doi: 10.1002/admt.201800336.

[15] H. Song, S. Timilsina, J. Jung, T. S. Kim, and S. Ryu, 'Improving the Sensitivity of the Mechanoluminescence Composite through Functionalization for Structural Health Monitoring', *ACS Appl Mater Interfaces*, vol. 14, no. 26, pp. 30205–30215, Jul. 2022, doi: 10.1021/acsami.2c07286.

[16] J. Zhao, S. Song, X. Mu, S. M. Jeong, and J. Bae, 'Programming mechanoluminescent

behaviors of 3D printed cellular structures', *Nano Energy*, vol. 103, Dec. 2022, doi: 10.1016/j.nanoen.2022.107825.

[17] D. K. Patel, B. El Cohen, L. Etgar, and S. Magdassi, 'Fully 2D and 3D printed anisotropic mechanoluminescent objects and their application for energy harvesting in the dark', *Mater Horiz*, vol. 5, no. 4, pp. 708–714, Jul. 2018, doi: 10.1039/c8mh00296g.

[18] M. Jayashuriya, S. Gautam, A. N. Aravinth, G. Vasanth, and R. Murugan, 'Studies on the effect of part geometry and process parameter on the dimensional deviation of additive manufactured part using ABS material', *Progress in Additive Manufacturing*, vol. 7, no. 6, pp. 1183–1193, Dec. 2022, doi: 10.1007/s40964-022-00292-9.

[19] A. Z. Farkas, S. V. Galatanu, and R. Nagib, 'The Influence of Printing Layer Thickness and Orientation on the Mechanical Properties of DLP 3D-Printed Dental Resin', *Polymers (Basel)*, vol. 15, no. 5, Mar. 2023, doi: 10.3390/polym15051113.

[20] A. Bagheri and J. Jin, 'Photopolymerization in 3D Printing', *ACS Applied Polymer Materials*, vol. 1, no. 4. American Chemical Society, pp. 593–611, Apr. 12, 2019. doi: 10.1021/acsapm.8b00165.

[21] Q. Zhang *et al.*, 'Design for the reduction of volume shrinkage-induced distortion in digital light processing 3D printing', *Extreme Mech Lett*, vol. 48, p. 101403, Oct. 2021, doi: 10.1016/j.eml.2021.101403.

[22] F. Jiang, A. Wörz, M. Romeis, and D. Drummer, 'Analysis of UV-Assisted direct ink writing rheological properties and curing degree', *Polym Test*, vol. 105, Jan. 2022, doi: 10.1016/j.polymertesting.2021.107428.

[23] 'Figure 4 ® MED-AMB 10 Biocompatible * Rigid HANDLING AND POST-PROCESSING GUIDELINES'. [Online]. Available: http://infocenter.3dsystems.comhttp://infocenter.3dsystems.com/figure4standalone/node

/1546http://infocenter.3dsystems.com/figure4modular/node/1741

[24] R. Raj, A. R. Dixit, S. S. Singh, and S. Paul, 'Print parameter optimization and mechanical deformation analysis of alumina-nanoparticle doped photocurable nanocomposites fabricated using vat-photopolymerization based additive technology', *Addit Manuf*, vol. 60, Dec. 2022, doi: 10.1016/j.addma.2022.103201.

[25] L. Schittecatte, V. Geertsen, D. Bonamy, T. Nguyen, and P. Guenoun, 'From resin formulation and process parameters to the final mechanical properties of 3D printed acrylate materials', *MRS Commun*, vol. 13, no. 3, pp. 357–377, Jun. 2023, doi: 10.1557/s43579-023-00352-3.

[26] J. J. Laureto and J. M. Pearce, 'Anisotropic mechanical property variance between ASTM D638-14 type i and type iv fused filament fabricated specimens', *Polym Test*, vol. 68, pp. 294–301, Jul. 2018, doi: 10.1016/j.polymertesting.2018.04.029.

[27] A. Millero, C. Brown2, and G. Warner3, 'Guidance on the Use of Existing ASTM Polymer Testing Standards for ABS Parts Fabricated Using FFF'.

[28] K. Park, C. Song, J. Park, and S. Ryu, 'Multi-objective Bayesian optimization for the design of nacre-inspired composites: optimizing and understanding biomimetics through AI', *Mater Horiz*, vol. 10, no. 10, pp. 4329–4343, Jun. 2023, doi: 10.1039/d3mh00137g.

[29] GPy, 'Gaussian process framework in Python, 2012', Accessed: May 10, 2024. [Online]. Available: URL https://github. com/SheffieldML/GPy.

[30] J. Lee *et al.*, 'Machine learning-based inverse design methods considering data characteristics and design space size in materials design and manufacturing: a review', *Materials Horizons*, vol. 10, no. 12. Royal Society of Chemistry, pp. 5436–5456, Aug. 04, 2023. doi: 10.1039/d3mh00039g.

[31] M. K. Kim *et al.*, 'Flexible submental sensor patch with remote monitoring controls for

management of oropharyngeal swallowing disorders', *Sci Adv*, vol. 5, no. 12, Dec. 2019, doi: 10.1126/sciadv.aay3210.

[32] J. Wang *et al.*, 'Screen-Printed Highly Sensitive and Anisotropic Strain Sensors With Asymmetrical Inner Concave Honeycomb Cross-Conducting Structure for Health Monitoring of Medical Electrophysiological Signals', *IEEE Sens J*, vol. 23, no. 21, pp. 25732–25748, Nov. 2023, doi: 10.1109/JSEN.2023.3303014.

[33] Y. Li, L. Shi, Y. Cheng, R. Wang, and J. Sun, 'Development of conductive materials and conductive networks for flexible force sensors', *Chemical Engineering Journal*, vol. 455. Elsevier B.V., Jan. 01, 2023. doi: 10.1016/j.cej.2022.140763.

[34] D. Stančeková *et al.*, 'Identification of the Production of Small Holes and Threads Using Progressive Technologies in Austenite Stainless Steel 1.4301', *Materials*, vol. 16, no. 19, Oct. 2023, doi: 10.3390/ma16196538.

[35] N. Römgens, A. Abbassi, C. Jonscher, T. Grießmann, and R. Rolfes, 'On using autoencoders with non-standardized time series data for damage localization', *Eng Struct*, vol. 303, Mar. 2024, doi: 10.1016/j.engstruct.2024.117570.

[36] B. Yuan, W. Sun, Y. Wang, R. Zhao, X. Mu, and Q. Sun, 'Study on bolt preload measurement: An error compensation model for ultrasonic detection based on solid coupling', *Measurement (Lond)*, vol. 221, Nov. 2023, doi: 10.1016/j.measurement.2023.113484.

[37] F. Jaberi, S. O. Movahed, and A. Ahmadpour, 'The Study on Titanium Dioxide-Silica Binary Mixture Coated $SrAl_2O_4 : Eu^{2+}, Dy^{3+}$ Phosphor as a Photoluminescence Pigment in a Waterborne Paint', *J Fluoresc*, vol. 29, no. 2, pp. 461–471, Mar. 2019, doi: 10.1007/s10895-019-02356-6.